Efficient Frequency Scaling Algorithm for Short-Range 3-D Holographic Imaging Based on a Scanning MIMO Array

Kai Tan, Xudong Chen, *Fellow, IEEE*, Shiyou Wu, and Guangyou Fang

***Abstract*—Millimeter wave (MMW) holographic imaging technology is widely used in plenty of short range applications like security and medical diagnosis. When combining with multiple-input-multiple-output (MIMO) array, such a technology can acquire precise reconstruction with wider field of view and higher dynamic range. However, to focus the higher-dimensional data set obtained from MIMO architecture, the complicated iteration or interpolation employed by the previous state-of-the-art focusing techniques prevents the real-time operation of such an imaging system under a general computation power. It is more economical to increase the operational speed by improving the algorithm efficiency. Hence, a novel fast imaging algorithm that uses multi-static frequency scaling technique is proposed in this paper for achieving real-time 3-D imaging on 1-D MIMO scanning system. Only FFT/IFFT and multiplications are employed in the algorithm, which can be easily implemented. Compared with the previous state-of-the-art techniques, the proposed algorithm has the lower computation complexity. Practical experiments with self-developed MMW MIMO scanning radar prove the accuracy and efficiency of the algorithm. On a common laptop without any acceleration technology, the proposed algorithm cost less than one tenth of the time required by the previous state-of-the-art techniques.**

***Index Terms*—3-D imaging, frequency scaling (FS), millimeter-wave (MMW) holographic imaging, multiple-input-multiple-output (MIMO), weapon detection.**

I. Introduction

Active millimeter wave (MMW) imaging architectures can achieve high resolution in azimuth by applying real aperture or synthetic aperture array, and high resolution in range by a certain frequency bandwidth. Besides, electromagnetic waves in MMW frequency band can also provide nice penetration ability, and therefore is vulnerable to the operational environment. Based on these characteristics and advantages, such a technology has received wide attention in recent years and has been employed in so many short-range sensing applications, such as free-space surveillance [1]-[3], through-the-wall detection [4], [5], security check [6]-[9], medical diagnosis [10], [11], biological detection [12], [13], etc. For these occasions, real-time and precise data processing is often necessary.

Recently, multiple-input-multiple-output (MIMO) technology is gradually brought into MMW imaging applications [14]-[19]. Compared with traditional mono-static mode, MIMO technology enjoys various benefits, such as wider field of view, higher dynamic range, saving hardware cost, etc. To get 3-D reconstruction under a common strip-map mode, it is obvious that a 2-D planar aperture is necessary to be formed. A 2-D real-aperture MIMO array would certainly be the most direct and ideal solution since it would not require any moving parts and could, therefore, even operate at video frame rates. In MMW frequency band, however, to cover a wide detection region, where the sampling with the spacing that about one-wavelength is required, the cost and complexity of a large 2-D MIMO real-aperture array renders it impractical at present time. By contrast, a 1-D linear MIMO array can be fabricated at reasonable cost, and also can be scanned quickly to gather full-aperture data. This paper studies exactly such a MIMO scanning regime.

Besides the hardware construction, imaging algorithm is also very important to the MMW imaging system as it not only determines imaging accuracy but also affects, to a great degree, the computation speed. So far, various MIMO imaging algorithms are studied in many literatures. The most traditional and optimum way is the time reversal techniques [8], [20], [21]. However, in the face of large-size data and high number of voxels, the great number of iteration operations in such algorithms will cost a huge amount of computation time even on a powerful computation platform. By contrast, the Fourier domain focusing techniques are much more preferred. However, those planar array based imaging algorithms [22]-[27] cannot be applied directly to the scanning regime studied here, as their forward wave models are completely different with each other. In addition, the phase center based techniques [14], [19] are also not discussed here, as the far-field condition will introduce significant focusing error when the spacing between transmitter and receiver is comparable with target distance. For precise 1-D MIMO scanning model, [28] first proposed a range migration algorithm (RMA). A novel multi-static Stolt interpolation is employed to compensate the range curvature in scanning MIMO wave data. Then, a MIMO enhanced algorithm (MIMO-EA) was studied in [29], and a SAR-FFT algorithm was developed in [30]. In these two algorithms, the focusing for scanning MIMO data set is realized successively at each

Manuscript received January 10, 2020; revised March 12, 2020. This work was supported in part by the National Natural Science Foundation of China under Grant 61501424 and Grant 61531018.

K. Tan and X. Chen are with the Department of Electrical and Computer Engineering, National University of Singapore, Singapore 117583 (e-mail: eletanka@nus.edu.sg; elechenx@nus.edu.sg).

S. Wu and G. Fang are with the Key Laboratory of Electromagnetic Radiation and Sensing Technology, Chinese Academy of Sciences, Beijing 100190, China (e-mail: ahwushiyou@126.com; gyfang@mail.ie.ac.cn).

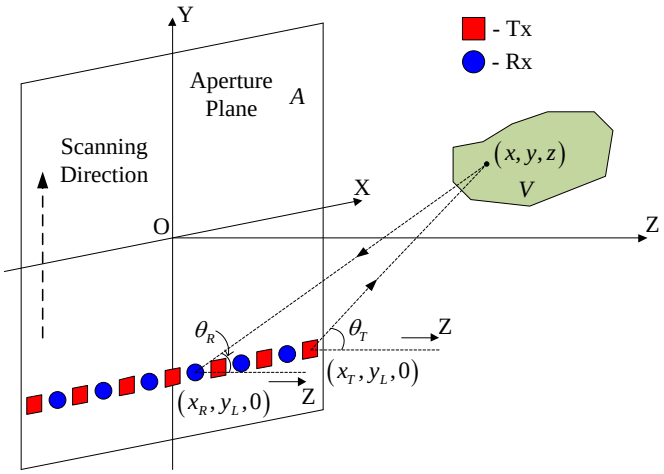

Fig. 1. Short-range sensing based on a 1-D MIMO scanning array.

frequency point and each transmitter location. Experimental results show that accurate 3-D imaging can be realized on 1-D MIMO scanning system by using these Fourier domain techniques, and their efficiency is much better than the time reversal technique. However, without exception, all these three algorithms must apply either interpolation or iteration operations. The effect of such operations for processing higher-dimensional MIMO data set is much more severe than mono-static case. In practical application with a common computation power, the running time required by these algorithms is a little high, and thus there is still a certain distance away from real-time operation, unless acceleration or parallel computation technology can be used.

It is more economical to enhance the system operational speed by improving algorithm efficiency than by upgrading hardware configures. Therefore, this paper is aimed at developing a precise imaging algorithm for 1-D MIMO scanning based imaging application, by which 3-D holographic reconstruction can be obtained in real time even on a common computation platform without using any acceleration technology. For achieving this purpose, a novel appropriate expansion is first given to the coupling phase of the 4-D MIMO data set. Then, the range-variable range cell migration (RCM) can be separated out and is corrected by a novel multi-static frequency scaling (FS) technique. The developed algorithm employs only fast Fourier transform (FFT) or inverse FFT (IFFT) and multiplication operations. The computation complexity of the algorithm is $O\left(N^4 \log_2 N\right)$, which is lower than the previous state-of-the-art algorithms. Besides, for our practical measurement geometry with 10^o squint, the focusing error caused by the phase expansion is lower than 0.02π, which has no negative effects on imaging quality. Additionally, the proposed algorithm is not limited to the application on evenly arranged array, but also suitable for non-uniform or even random configuration. Practical measurements prove the nice imaging quality acquired by the algorithm, and in the meanwhile, the computation time is much less than that required by the previous state-of-the-art algorithms.

The rest of this paper is organized as follows. Section II studies the principle of the 3-D inversion by the novel MIMO-FS algorithm (MIMO-FSA). Section III discusses the implementation details, computation complexity and focusing error of the algorithm. Section IV is the validation, where the performance of the algorithm is compared with the previous state-of-the-art algorithms first by point-target simulation and then by the practical measurements on a MMW MIMO scanning radar system. Finally, Section V concludes this paper.

II. MIMO Scanning Imaging with MIMO-FSA

This section first derives the forward wave model under 1-D MIMO scanning geometry. Based on that, 3-D inversion is then formulated by applying the novel MIMO-FSA.

A. Imaging Model

Firstly, it is necessary to establish the studied measurement geometry and formulate the corresponding wave spectrum, which is the basis of the following reconstruction work. Consider the short-range imaging geometry given in Fig. 1. The target is illuminated by a linear MIMO array, which is arranged in the horizontal direction X and scans along the height direction Y. The locations of the transmitter and receiver are denoted as $\left(x_T, y_L, 0\right)$ and $\left(x_R, y_L, 0\right)$, respectively, while the target area is represented by $o\left(x, y, z\right)$. Then, θ_T and θ_R denote the sensing squints. In order to obtain the 3-D reconstruction for the space with a certain depth of field (DOF), the transmitted wave field must possess a certain frequency bandwidth, and here assume the transmitted wave has the amplitude spectrum of $P(\bullet)$. Under the first-order Born approximation [20], the frequency domain received wave field that corresponds to the transceiver pair $\left(x_T, x_R; y_L\right)$ in Fig. 1 can be obtained as

$$\begin{aligned} &sS\left(x_T, x_R; y_L; k\right) \\ &= \iiint_V dxdydz \frac{w_T\left(x-x_T, y-y_L\right) w_R\left(x-x_R, y-y_L\right)}{4\pi R_T R_R} \\ &\quad \times f\left(x, y, z\right) P\left(k\right) \exp\left[-j\left(k_0+k\right)\left(R_T+R_R\right)\right] \end{aligned} \tag{1}$$

where $f\left(x, y, z\right)$ denotes the target reflectivity map, k_0 is the wavenumber corresponding to the center frequency, k is the baseband wavenumber, $w_T(\bullet)$ and $w_R(\bullet)$ denote the azimuth weight functions that are brought by the radiation patterns of the used transmitter and receiver, respectively, and

$$\begin{aligned} R_T &= \sqrt{\left(x-x_T\right)^2+\left(y-y_L\right)^2+z^2} \\ R_R &= \sqrt{\left(x-x_R\right)^2+\left(y-y_L\right)^2+z^2} \end{aligned} \tag{2}$$

are the range histories of the transmitter and receiver, respectively. Note that the spreading losses due to the propagation are taken into consideration in (1) because of the short-range sensing nature of the measurement geometry. Another thing to note is that in the wave function name, the case of letter is used to distinguish the domain that the wave belongs to. The uppercase denotes Fourier domain while the lowercase means time domain, and the former letter denotes azimuth while the latter means range. Such a kind of expression will still be used throughout the paper.

To get the ω-K domain spectrum, conduct a 3-D Fourier transform (FT) to the wave in (1) and use the principle of stationary phase (PSP) to solve the Fourier integral. Then, the

wave spectrum can be obtained as

$$\begin{aligned} &SS\left(k_{xT},k_{xR};k_y;k\right)\\ &=\iiint_A dx_T dx_R dy_L \times sS\left(x_T,x_R,y_L;k\right)\\ &\quad\times\exp\left[-j\left(k_{xT}x_T+k_{xR}x_R+k_y y_L\right)\right]\\ &=\iiint_V dxdydz\times f\left(x,y,z\right)A\left(k_{xT},k_{xR};k_y;k\right)\\ &\quad\times\exp\left\{-j\left[\left(k_{xT}+k_{xR}\right)x+k_y y\right]\right\}\exp\left[-j\sqrt{k_{yz}^2-k_y^2}z\right] \end{aligned} \tag{3}$$

where k_{xT} , k_{xR} , k_y are the azimuth wavenumbers, and $k_{yz}=\sqrt{\left(k_0+k\right)^2-k_{xT}^2}+\sqrt{\left(k_0+k\right)^2-k_{xR}^2}$, and the amplitude function is given as

$$\begin{aligned} &A\left(k_{xT},k_{xR};k_y;k\right)\\ &=\frac{P(k)}{\sqrt{z}\left\{\left[\left(k_0+k\right)^2-k_{xT}^2\right]\left[\left(k_0+k\right)^2-k_{xR}^2\right]\left(k_{yz}^2-k_y^2\right)\right\}^{1/4}}\\ &\quad\times w_T\left[\frac{k_{xT}k_{yz}z}{\sqrt{\left(k_0+k\right)^2-k_{xT}^2}\sqrt{k_{yz}^2-k_y^2}},\frac{k_y z}{\sqrt{k_{yz}^2-k_y^2}}\right]\\ &\quad\times w_R\left[\frac{k_{xR}k_{yz}z}{\sqrt{\left(k_0+k\right)^2-k_{xR}^2}\sqrt{k_{yz}^2-k_y^2}},\frac{k_y z}{\sqrt{k_{yz}^2-k_y^2}}\right] \end{aligned} \tag{4}$$

The detailed acquirement of the wave expression in (3) is given in APPENDIX A.

After applying the azimuth frequency relation [22]

$$k_x \triangleq k_{xT}+k_{xR} \tag{5}$$

it is clear that (3) is a simple 3-D FT, and thus the reflectivity function can be reconstructed by a 3-D inverse FT (IFT) [28]. However, to fulfill this 3-D IFT, a 1-D interpolation over the range dimension is necessary to realize the uniform sampling on this dimension, which is the well-known Stolt interpolation. It can be found that the coefficient of such an interpolation must update constantly over all four dimensions during the interpolating procedure. Hence, it will give heavy computation burden for the 4-D data processing.

In order to avoid the complicated Stolt interpolation, a novel expansion is given to the coupling phase term, i.e., the second phase term in (3), as

$$\sqrt{k_{yz}^2-k_y^2}z\approx\left(g_0+g_1k\right)z \tag{6}$$

where the coefficients are given as

$$g_0=k_0D_Y\left(D_{Tx}+D_{Rx}\right)\quad g_1=\frac{D_{Tx}+D_{Rx}}{D_{Tx}D_{Rx}D_Y} \tag{7}$$

where D_{Tx} , D_{Rx} and D_Y are the range-Doppler (R-D) domain cosine functions of the squints, i.e.,

$$\begin{aligned} &D_{Tx}=\sqrt{1-k_{xT}^2/k_0^2}\quad D_{Rx}=\sqrt{1-k_{xR}^2/k_0^2}\\ &D_Y=\sqrt{1-\frac{k_y^2}{k_0^2\left(D_{Tx}+D_{Rx}\right)^2}} \end{aligned} \tag{8}$$

The details of such an expansion can be found in APPENDIX B. In (6), g_0z denotes the azimuth modulation while the first-order term g_1kz represents the key RCM. Note that, both of these phase terms are range-dependent.

B. Inversion by MIMO-FSA

Then, the 3-D inversion is formulated by introducing the novel multi-static FS technique. According to the expansion of (6), it is obvious that the azimuth modulation can be easily compensated by a matched filter in R-D domain, and thus our primary mission is to correct the range-dependent RCM term.

1. Reference function multiplication (RFM)

Define the ω-K domain RFM function as

$$H_{RFM}\left(k_{xT},k_{xR};k_y;k\right)=\frac{1}{A}\exp\left[j\sqrt{k_{yz}^2-k_y^2}z_0\right] \tag{9}$$

where z_0 is the range of the target center. Then, conduct the RFM filtering,

$$\begin{aligned} &SS_1\left(k_{xT},k_{xR};k_y;k\right)\\ &=SS\times H_{RMF}\\ &\approx\iiint_V dxdydz\times f\left(x,y,z\right)\\ &\quad\times\exp\left\{-j\left[\left(k_{xT}+k_{xR}\right)x+k_y y\right]\right\}\\ &\quad\times\exp\left[-j\left(g_0+g_1k\right)\left(z-z_0\right)\right] \end{aligned} \tag{10}$$

Such an RFM filtering is to achieve the bulk correction, including the bulk azimuth compression (AC), bulk RCM correction (RCMC) and bulk second range compression (SRC). The residual coupling will be further corrected by the following steps.

2. Introducing residual video phase (RVP)

This operation is to introduce the RVP term, which is necessary for the RCMC by the subsequent multi-static FS operation. Define the RVP function with the characteristic of linear frequency modulation (LFM) as

$$h_{RVP}\left(t\right)=\exp\left(jKt^2\right) \tag{11}$$

where $K=\pi B\times df$ (B and df denote the width and sampling interval of the working frequency band, respectively) is the frequency modulation (FM) rate. Then, conduct the R-D domain filtering,

$$Ss_2\left(k_{xT},k_{xR};k_y;t\right)=h_{RVP}\int SS_1\exp\left(jckt\right)dk \tag{12}$$

According to convolution theorem, the range FT of Ss_2 can be obtained as

$$\begin{aligned} &SS_2\left(k_{xT},k_{xR},k_y;k\right)\\ &=SS_1\otimes\int h_{RVP}\exp\left(-j\omega t\right)dt\\ &=\iiint_V dxdydz\times f\left(x,y,z\right)\\ &\quad\times\exp\left\{-j\left[\left(k_{xT}+k_{xR}\right)x+k_y y\right]\right\}\\ &\quad\times\exp\left[-j\left(g_0+g_1k\right)\left(z-z_0\right)\right]\otimes\exp\left(-j\frac{c^2k^2}{4K}\right) \end{aligned} \tag{13}$$

where $\otimes$ represents the convolution operation.

3. Multi-static FS

This operation is to accomplish the key differential RCMC, i.e., to correct the first-order term of k in (13). Define the FS function as

$$H_{FS}\left(k_{xT},k_{xR};k_y;k\right)=\exp\left[j\frac{c^2k^2}{4K}\left(1-\xi\right)\right] \tag{14}$$

where $\xi=\frac{2D_{Tx}D_{Rx}D_Y}{D_{Tx}+D_{Rx}}$. It is clear that H_{FS} also has the property of LFM. However, its FM rate, i.e., $K/\left(\xi-1\right)$, is a function of azimuth frequency. Then, conduct the multi-static FS to the wave of (13) and yield

$$\begin{aligned}&SS_3\left(k_{xT},k_{xR};k_y;k\right)\\&=SS_2\times H_{FS}\\&=\iiint_V dxdydz\times\xi f\left(x,y,z\right)\\&\quad\times\exp\left\{-j\left[\left(k_{xT}+k_{xR}\right)x+k_yy+2k\left(z-z_0\right)\right]\right\}\\&\quad\times\exp\left[-jg_0\left(z-z_0\right)\right]\\&\quad\times\exp\left[j\frac{c^2\xi k^2}{4K}\left(1-\xi\right)\right]\otimes\exp\left(-j\frac{c^2\xi k^2}{4K}\right)\end{aligned} \tag{15}$$

The derivation for (15) is given in APPENDIX C.

4. RVP correction (RVPC)

Define the RVPC function as

$$h_{RVPC}\left(k_{xT},k_{xR};k_y;t\right)=\frac{1}{\xi}\exp\left(-j\frac{K}{\xi}t^2\right) \tag{16}$$

and conduct the R-D domain matched filtering,

$$Ss_4\left(k_{xT},k_{xR};k_y;t\right)=h_{RVPC}\int SS_3\exp\left(jckt\right)dk \tag{17}$$

According to convolution theorem, the range FT of Ss_4 can be obtained as

$$\begin{aligned}&SS_4\left(k_{xT},k_{xR};k_y;k\right)\\&=\iiint_V dxdydz\times f\left(x,y,z\right)\\&\quad\times\exp\left\{-j\left[\left(k_{xT}+k_{xR}\right)x+k_yy+2k\left(z-z_0\right)\right]\right\}\\&\quad\times\exp\left[-jg_0\left(z-z_0\right)\right]\exp\left[j\frac{c^2\xi k^2}{4K}\left(1-\xi\right)\right]\end{aligned} \tag{18}$$

After this RVPC, the RVP term in (15), i.e., the convolution term, is removed.

5. *Inverse FS (IFS)*

Define the IFS function as

$$H_{IFS}\left(k_{xT},k_{xR};k_y;k\right)=\exp\left[j\frac{c^2\xi k^2}{4K}\left(\xi-1\right)\right] \tag{19}$$

Then, conduct the ω-K domain filtering, we have

$$\begin{aligned}&SS_5\left(k_{xT},k_{xR};k_y;k\right)\\&=SS_4\times H_{IFS}\\&=\iiint_V dxdydz\times f\left(x,y,z\right)\exp\left[-jg_0\left(z-z_0\right)\right]\\&\quad\times\exp\left\{-j\left[\left(k_{xT}+k_{xR}\right)x+k_yy+2k\left(z-z_0\right)\right]\right\}\end{aligned} \tag{20}$$

6. Differential AC

In (20), it is clear that after decoupling, k and $2z$ (since k is the one-way wavenumber) are now an FT pair, thus z can be reconstructed by a range IFT,

$$\begin{aligned}&Ss_5\left(k_{xT},k_{xR},k_y;z\right)\\&=\iint_V dxdy\times f\left(x,y,z\right)\exp\left[-jg_0\left(z-z_0\right)\right]\\&\quad\times\exp\left\{-j\left[\left(k_{xT}+k_{xR}\right)x+k_yy\right]\right\}\end{aligned} \tag{21}$$

Define the differential AC function as

$$h_{AC}\left(k_{xT},k_{xR},k_y;z\right)=\exp\left[jg_0\left(z-z_0\right)\right] \tag{22}$$

and conduct the differential AC in R-D domain and yield

$$\begin{aligned}&Ss_6\left(k_{xT},k_{xR};k_y;z\right)\\&=Ss_5\times h_{AC}\\&=\iint_V dxdy\times f\left(x,y,z\right)\exp\left\{-j\left[\left(k_{xT}+k_{xR}\right)x+k_yy\right]\right\}\end{aligned} \tag{23}$$

So far in (23), the range-dependent azimuth modulation and RCM are completely compensated, which means that the range and azimuth in the wave data have been decoupled from each other. Then, by using the azimuth relation defined in (5), (23) represents a 2-D FT relation, and thus the 3-D reflectivity function can finally be reconstructed with a 2-D IFT as

$$\begin{aligned}&f\left(x,y,z\right)\\&=\iint_W Ss_6\left(k_x,k_y;z\right)\exp\left[j\left(k_xx+k_yy\right)\right]dk_xdk_y\end{aligned} \tag{24}$$

where W denotes the wavenumber space.

III. IMPLEMENTATION, COMPLEXITY AND ERROR

This section mainly discusses the implementation details, computation load and focusing error of the proposed algorithm.

A. Algorithm Implementation

According to the inversion process formulated in Section II, the focusing steps of the developed MIMO-FSA can be obtained as shown in Fig. 2. It can be seen that the algorithm needs totally seven FFT/IFFT and six multiplications to realize the 3-D reconstruction, no any interpolation or iteration is used.

When applying the algorithm, there are two things that should be noted. First, in order to ensure that the wave data is evenly sampled at k_x dimension after taking the transform of (5), k_{xT} and k_{xR} must have the same sampling interval. Hence, the transmit and receive arrays in the applied 1-D MIMO array should have the same width. In practical application, if such a condition cannot be met, then proper zero-padding should be performed prior to the 3-D azimuth FFT operation so that the following relation can be satisfied:

$$\left(N_{xT}-1\right)\bar{d}_{xT}=\left(N_{xR}-1\right)\bar{d}_{xR} \tag{25}$$

where N_{xT} and N_{xR} are the number of samples in the transmit and receive arrays, and $\bar{d}_{xT}$ and $\bar{d}_{xR}$ are the average sampling intervals in the transmit and receive arrays, respectively.

Second, according to the discussion in [29], the equivalent aperture of the used MIMO array should satisfy the sampling criteria given in [29]. However, it is clear that the equivalent aperture can have an arrangement that meets the sampling criteria even if the real MIMO array has a sparse transmit or receive sub-array. Conducting directly the 3-D azimuth FFT to such a sparsely arranged MIMO data set will certainly cause aliasing in the final image. To have an accurate imaging result,

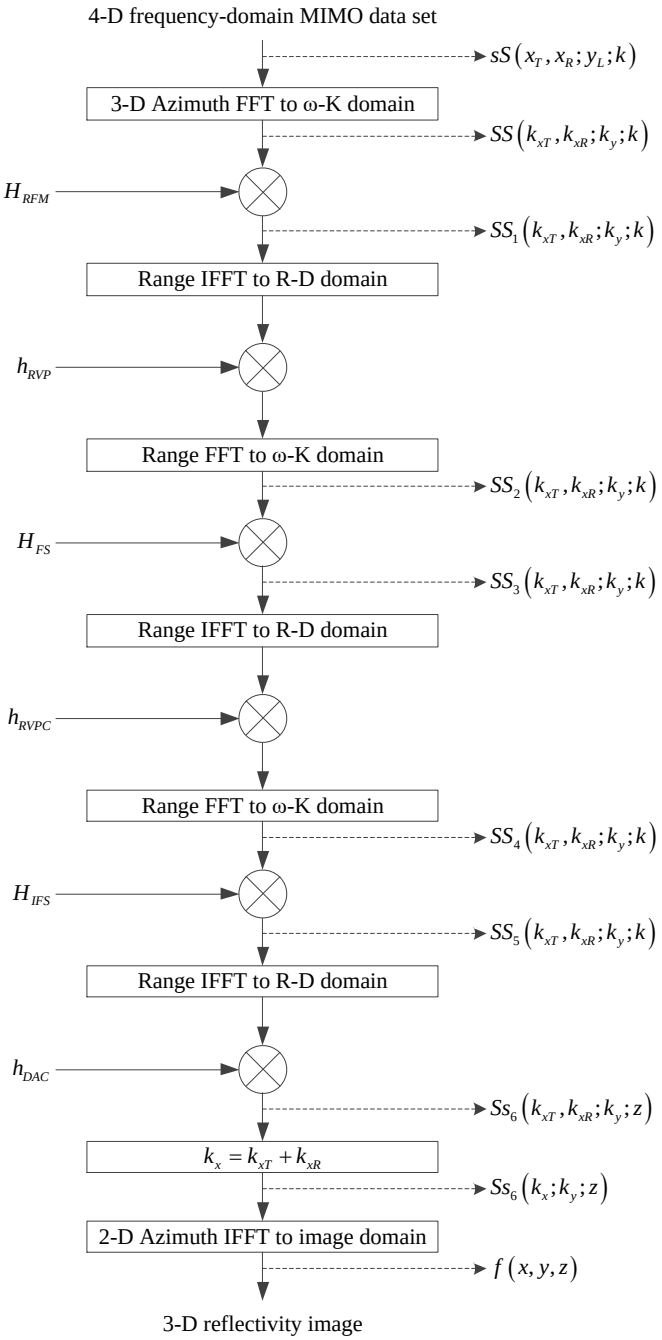

Fig. 2. Block scheme of MIMO-FSA for 1-D MIMO scanning based 3-D imaging.

proper zero-padding can be carried out for the original data set before taking the azimuth FFT. It is clear that this operation does not have any side effect for the following focusing procedure. In addition, through the zero-padding with an appropriate spacing, the proposed algorithm is not limited to evenly arranged MIMO array, but can also be applied to other non-uniform or even random configurations.

B. Computation Complexity

The computation load is measured by the floating-point operations (FLOPs). Let N_{xT}, N_{xR}, N_y and N_s represent the number of samples (after zero-padding if it is needed) over the four dimensions, $N_x = N_{xT} + N_{xR} - 1$ is the azimuth samples after taking the azimuth transform of (5), N_{Tx} is the number of the used transmitting antennas in the MIMO array, and N_{Iz} is the number of voxels in range direction of the 3-D focused image. The computation load of the proposed algorithm and the three previous state-of-the-art imaging techniques, i.e., RMA [28], SAR-FFT [30] and MIMO-EA [29], are summarized in TABLE I.

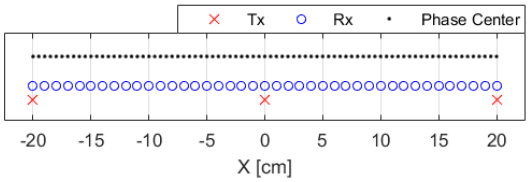

Fig. 3. MIMO array applied in point target simulation. Equivalent aperture is evenly arranged with 5-mm interval, which meets sampling criterion.

TABLE I
COMPUTATION LOAD OF FOUR ALGORITHMS

Algorithm	FLOPs
Proposed MIMO-FSA	$5N_{xT}N_{xR}N_yN_s\log_2\left(N_{xT}N_{xR}N_yN_s^5\right)$ $+38N_{xT}N_{xR}N_yN_s+5N_xN_yN_s\log_2\left(N_xN_y\right)$
RMA	$5N_{xT}N_{xR}N_yN_s\log_2\left(N_{xT}N_{xR}N_y\right)$ $+(8+C)N_{xT}N_{xR}N_yN_s+5N_xN_yN_s\log_2\left(N_xN_yN_s\right)$
SAR-FFT	$N_sN_{Tx}\left(\begin{matrix}5N_{xR}N_y\log_2 N_y+6N_{xR}N_yN_{Iz}\\+5N_{xR}N_yN_{Iz}\log_2 N_y\end{matrix}\right)$ $+6N_{Tx}N_sN_{xR}N_yN_{Iz}+6N_sN_{xR}N_yN_{Iz}$
MIMO-EA	$N_{Tx}N_yN_s\left(5N_{Iz}N_{xR}\log_2 N_{xR}+18N_{Iz}N_{xR}\right)$ $+5N_{Tx}N_yN_sN_{xR}\left(\log_2 N_{xR}+\log_2 N_y\right)$

In TABLE I, the computation load for FFT/IFFT and multiplication is well studied in [31]. While for conducting the azimuth relation of (5), $N_{xT}N_{xR}N_yN_s$ complex add operations are required. The RMA needs to carry the Stolt interpolation, and C represents the calculation amount of the 1-D interpolation operation for each source point. C is related to the used interpolation method and specific implementation. A 1-D Stolt interpolation is in effect a complicated convolution process [31], which requires not only the essential multiplication and sum operations, but also other auxiliary operations, such as the search for the interpolating location, the calculation of coefficient (or through table lookup), etc. By contrast, the FFT and multiplications employed in the proposed algorithm are much more straightforward, no any auxiliary operations are required.

To compare the complexity of the four algorithms intuitively, suppose that all the parameters are in the same order with a given number N. Then, the computation complexities of the four algorithms listed in TABLE I are $O\left(N^4\log_2 N\right)$, $O\left[N^4\left(C+\log_2 N\right)\right]$, $O\left(N^5\log_2 N\right)$ and $O\left(N^5\log_2 N\right)$, respectively. It is clear that the proposed algorithm enjoys the lowest complexity. Its superiority on computation efficiency will be further shown in the following measurements.

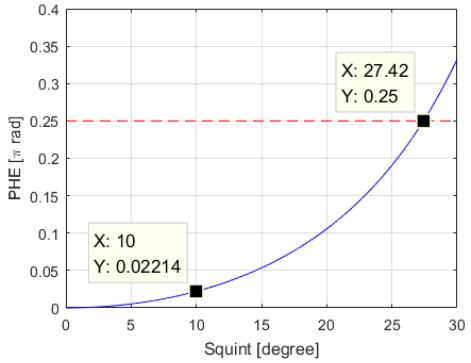

Fig. 4. Phase error of MSFSA changed with sensing squint when frequency band is from 27 GHz to 33 GHz and target depth is 0.5 m.

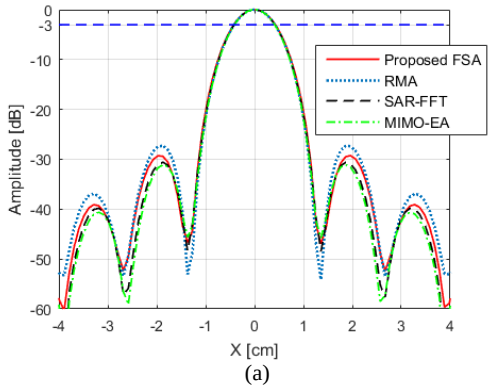

Fig. 5. Profiles of PSF patterns obtained by four algorithms. (a) Profiles along horizontal X direction. (b) Profiles along vertical Y direction.

C. Focusing Error

It is clear that the focusing error mainly comes from the applied phase expansion in (6), therefore, by comparing the two sides of (6), the phase error can be easily acquired as

$$PHE = \left| \left[\sqrt{k_{yz}^2 - k_y^2} - \left(g_0 + g_1 k \right) \right] \left(z - z_0 \right) \right| \tag{26}$$

Such a phase error is related to the bandwidth, sensing squint and DOF. Take the following experiment as an example. The center frequency is 30 GHz, with the bandwidth of 6 GHz, the maximum squint of the applied antenna is about 10^o, and the target depth is less than 0.5 m. Under such parameters, the maximum phase error acquired by (26) is only about 0.02π, which is quite acceptable for precise imaging. Furthermore, with the same operational band and target depth, the phase error changed with sensing squint is plotted in Fig. 4. The maximum allowable for accurate imaging, i.e., the corresponding phase error should be lower than 0.25π [31], is about 27^o. Such a high squint is sufficient to meet the requirements of most short-range imaging applications.

TABLE II
PSL AND BEAMWIDTH OF THE PATTERNS IN Fig. 5 (a)

Algorithm	PSL	-3-dB beamwidth
MIMO-FSA	-29.25 dB	0.86 cm
RMA	-27.27 dB	0.84 cm
SAR-FFT	-30.59 dB	0.83 cm
MIMO-EA	-31.08 dB	0.82 cm

TABLE III
PSL AND BEAMWIDTH OF THE PATTERNS IN Fig. 5 (b)

Algorithm	PSL	-3-dB beamwidth
MIMO-FSA	-20.74 dB	0.68 cm
RMA	-20.49 dB	0.68 cm
SAR-FFT	-21.69 dB	0.68 cm
MIMO-EA	-22 dB	0.67 cm

IV. RESULTS

Both numerical simulation and practical measurements are conducted to evaluate the imaging performance of the proposed MIMO-FSA. All the algorithms are realized by MATLAB codes at a common laptop that is equipped with a 64-bit 2.20-GHz Intel Core I7-8750H CPU. No any acceleration or parallel technique is used. In addition, considering both accuracy and efficiency, a linear interpolator is applied in RMA to fulfill the Stolt interpolation.

A. Point Spread Function (PSF)

The PSF pattern is a useful tool to measure the focusing performance, and thus the PSF pattern is first analyzed by conducting numerical simulation with point-like target. In the measurement, a 1-cm-diameter metal sphere is illuminated by a scanning linear MIMO array with the distance of 0.5 m. The width of the MIMO array is 0.4 m, while the interval between antennas is 0.2 m and 0.01 m for the transmit and receive array, respectively. The configuration of the used MIMO array is displayed in Fig. 3. The spacing of the equivalent aperture is 5 mm, which is sufficient to achieve the accurate focusing without any aliasing. The antennas with 20^o beamwidth are applied in the MIMO array. The transmitted wave field has the center frequency of 30 GHz with the 6-GHz bandwidth. Such system parameters are almost the same as our following practical experiments. The scattered field is computed by the simulation tool FEKO.

In order to give a quantitative study of the PSF pattern, the profiles of the pattern along different directions should be provided, which are obtained by the following way. 3-D image is first numerically calculated by the algorithm. Then, maximum projection is given to the 3-D result to get the 2-D azimuth pattern. Finally, another maximum projection is given to the 2-D pattern along horizontal X or vertical Y direction to get the 1-D profiles. Note that the original wave data should take a proper zero-padding when using the proposed algorithm, as the transmit array has a sparse arrangement. The azimuth

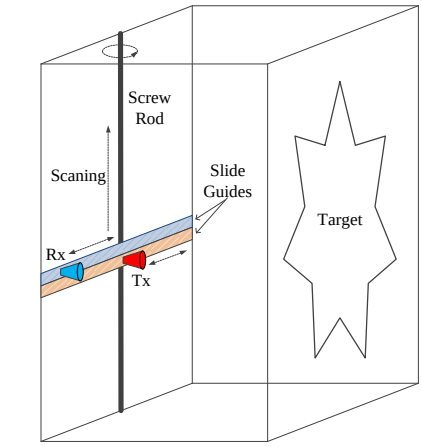

(a)

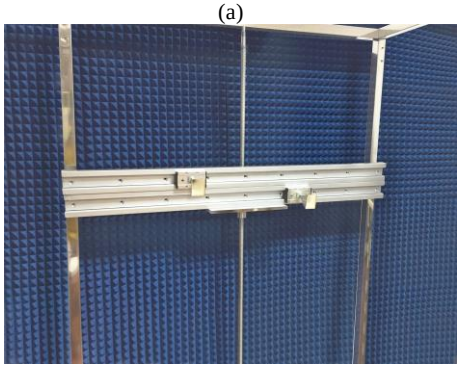

(b)

Fig. 6. (a) Schematic diagram of applied MIMO scanning mechanism. (b) Photograph of applied MIMO scanner, which has two horizontal slide guides fixed on a vertical screw rod to realize 1-D MIMO array scanning.

TABLE IV
SETTINGS FOR THE MEASUREMENTS

System parameter	Experiment #1	Experiment #2
Center frequency	30 GHz	30 GHz
Bandwidth	6 GHz	6 GHz
Frequency interval	150 MHz	150 MHz
Tx width	0.4 m	0.8 m
Tx spacing	0.2 m	0.2 m
Rx width	0.4 m	0.8 m
Rx spacing	0.01 m	0.01 m
Scanning height	0.4 m	2 m
Scanning interval	0.01 m	0.01 m
Imaging cube	0.4 m × 0.4 m × 1 m	0.8 m × 2 m × 1 m
Image voxel	401 × 401 × 101	801 × 2001 × 101

profiles along horizontal and vertical directions are displayed in Fig. 5, where the results by the previous state-of-the-art RMA, SAR-FFT and MIMO-EA are also given for comparison. Furthermore, the values of the peak sidelobe level (PSL) and -3-dB beamwidth of the patterns in Fig. 5 are summarized in TABLE II and TABLE III.

From Fig. 5, TABLE II and TABLE III, it is clear that the focusing performance of the proposed algorithm is as good as the three previous state-of-the-art algorithms. Compared with the optimum MIMO-EA, the proposed MIMO-FSA suffers a tiny loss in both sidelobe level and -3-dB resolution. However, such a small degradation will not bring any negative effect for the imaging with complex targets.

B. Practical Experiment

The proposed MIMO-FSA is further verified experimentally by a self-developed MMW MIMO scanning system. The block

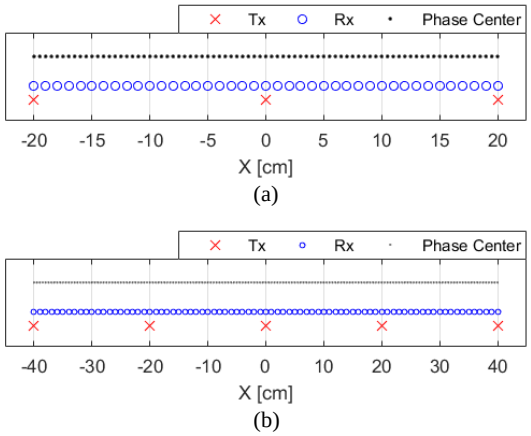

Fig. 7. Applied MIMO arrays for (a) first measurement with sheets pattern and (b) second measurement with human body. Two arrays have the same topology but only with different sizes. Equivalent apertures of both arrays are evenly arranged with 5-mm spacing, which satisfies sampling criterion.

diagram of such a system and the applied scanner are displayed in Fig. 6. In the scanner, two adjacent horizontal slide guides with slide blocks are fixed on a mechanical platform, which is situated on a vertical screw rod. Two antennas are fixed on the sliding blocks to transmit and receive electromagnetic waves at any horizontal positions. The screw rod can rotate at a certain rate to realize the horizontal platform move along the vertical direction. Based on such a mechanism, a MIMO scanning geometry that is equivalent to Fig. 1 is realized. In Fig. 6 (b), the used antennas are a kind of horn with a 3-dB bandwidth from 18 GHz to 40 GHz and a 22^{o} 3-dB beamwidth.

In the applied system, the transmitters are connected with an MMW oscillator to transmit waves that have a 6-GHz bandwidth on the center frequency of 30 GHz. The received signal is mixed with in-phase (0 phase shift) and quadrature (90 phase shift) signals coupled from the MMW oscillator, and then digitized with the frequency interval of 150 MHz. Such a signal is sampled over an $X-Y$ aperture by using the scanner to obtain the input frequency domain wave $sS\left(x_T, x_R; y_L; k\right)$. The proposed MIMO-FSA and the three previous state-of-the-art algorithms are then applied to reconstruct the 3-D image one after another. Two sets of experiments with different targets are conducted for our validation. The detailed settings for both measurements are summarized in TABLE IV. The MIMO arrays applied in the two measurements are shown in Fig. 7, which has exactly the same topology as the one employed in the former simulation. So, it is necessary to take a zero-padding before using the proposed algorithm. Here, the spacing of the zero-padding is 1 cm for the transmit array, i.e., the x_T-dimension in the 4-D MIMO data set.

The first target under test is a kind of sheets pattern. The photographs of the real object and measurement scenario are displayed in Fig. 8. The pattern is made by a group of narrow copper sheets with different gaps that from 3 mm to 10 mm. Such a pattern is a useful tool to measure the imaging resolution along both the array direction and the scanning direction. The 3-D holographic reconstructions by the four algorithms are shown in Fig. 9. All four algorithms give accurate reconstructions for the real pattern. To have a deeper sight for their resolving ability, the profiles of the reconstructed patterns

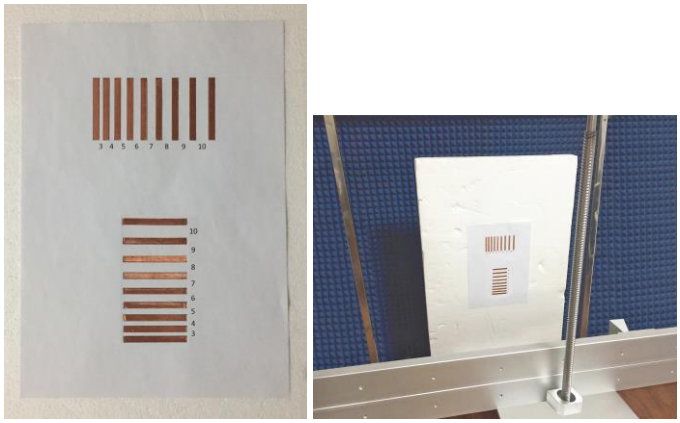

(a) (b)

Fig. 8. (a) Sheets pattern made by a set of copper sheets with the gaps from 3 mm to 10 mm. (b) Measurement scenario for the pattern. The pattern is 50-cm away from the scanning aperture.

are further provided in Fig. 10. The 3-dB gaps in Fig. 10 indicate that all four algorithms reach a resolution better than 8 mm in both the horizontal and vertical directions. Such performances basically agree with the simulated PSF patterns shown in Fig. 5.

The second target is a real person, who carries a plastic handgun on his left-hand-side waist. Such a human target is common in the short-range application like security check and it contains a certain DOF, which is sufficient to test the imaging accuracy at various distances. The measurement situation is shown in Fig. 10. In order to cover the full body of the person, the vertical scanning range is 2 m for this measurement. The reconstructed 3-D images for the full body are displayed in Fig. 12, and the place of the handgun is further zoomed in for a clear view. In Fig. 12, all four algorithms give accurate reconstruction for the human target. The fine parts, like the hands, face, and handgun, are all clearly reconstructed. Furthermore, it is clear that the proposed MIMO-FSA completely reaches the same imaging accuracy as the three previous state-of-the-art algorithms.

The computation time for these two groups of experiments are summarized in TABLE V. Since the data size for covering the full person is much larger than for the sheets pattern, the processing for the second experiment certainly costs more time. For both measurements, the proposed MIMO-FSA costs the least computation time. Due to the large number of iteration applied in SAR-FFT and MIMO-EA, much more time is required for their focusing procedure. While for RMA that needs to conduct Stolt interpolation, it costs the most time for the human reconstruction since a huge number of auxiliary operations are taken with the complicated interpolation. Note that, all these results are obtained only based on a common laptop without using any acceleration or parallel computation technology.

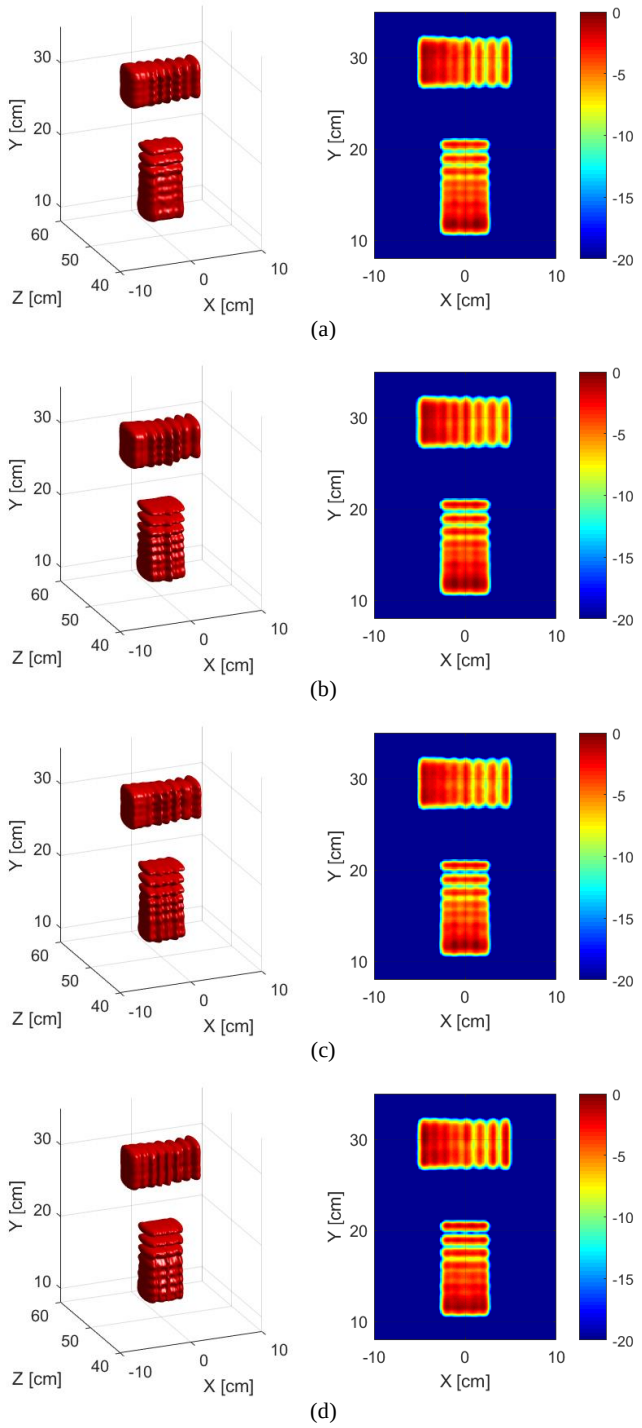

Fig. 9. Holographic reconstruction of sheets pattern shown in Fig. 8. (a) Reconstruction by proposed MIMO-FSA. (b) Reconstruction by RMA. (c) Reconstruction by SAR-FFT. (d) Reconstruction by MIMO-EA. All results are displayed under -20-dB level.

V. Conclusion

In this paper, a precise and efficient imaging algorithm is proposed for MMW 3-D holographic imaging based on 1-D MIMO scanning array. A novel expansion is carried out to the coupling phase of the 4-D MIMO data set. Based on such an expansion, a fast imaging algorithm that employs the novel multi-static FS technique is proposed for achieving the real-time imaging on 1-D MIMO scanning system. Only FFTs and multiplications are employed in the algorithm, and no any complicated interpolation or iteration is used. The computation complexity of the proposed algorithm is $O\left(N^4 \log_2 N\right)$, which is lower than the previous state-of-the-art algorithms. For validating the superiority of the algorithm, a 1-D MIMO scanning based MMW imaging system is developed. The phase error by using the algorithm is only 0.02π. Besides, the

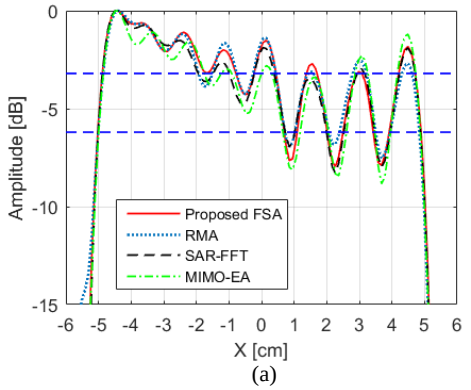

(a)

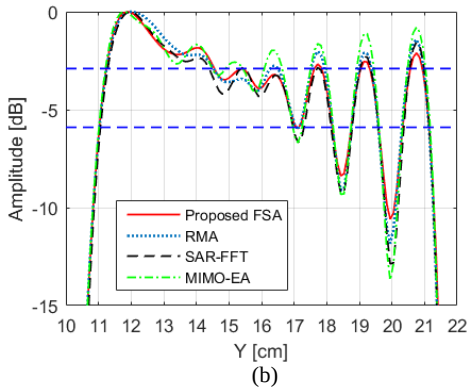

(b)

Fig. 10. Profiles of reconstructed patterns in Fig. 9. (a) Profiles of reconstructed vertical sheets. (b) Profiles of reconstructed horizontal sheets. The 3-dB gaps indicate the minimum resolved interval of 8 mm for both horizontal and vertical directions.

maximum allowable sensing squint under the same system setup is about 27^{o}, which is sufficient for most short-range imaging applications. With different targets, the imaging quality of the proposed algorithm, including the resolving ability and dynamic range, is demonstrated to reach completely the same level as the previous state-of-the-art algorithms. However, on a common laptop without using any acceleration technology, the proposed algorithm requires less than one tenth of the time as required by the previous state-of-the-art algorithms. The excellent imaging quality and computation speed indicate that real-time operation for 1-D MIMO scanning system can be realized by using the proposed algorithm even with a moderate computational device.

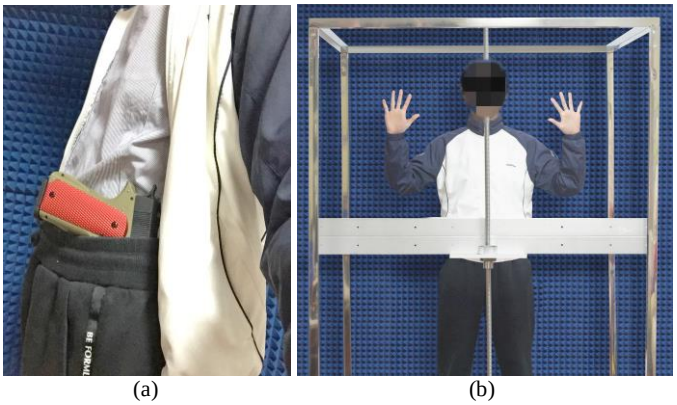

(a) (b)

Fig. 11. Measurement with a human body. (a) A plastic handgun is carried on his left hand side waist. (b) Measurement scenario. The person is about 50 cm away from the scanning aperture when being tested.

TABLE V
TIME REQUIRED BY FOUR ALGORITHMS

Algorithm	Experiment #1	Experiment #2
MIMO-FSA	0.5 s	5.3 s
RMA	5.1 s	98.8 s
SAR-FFT	10.0 s	94.1 s
MIMO-EA	9.8 s	92.6 s

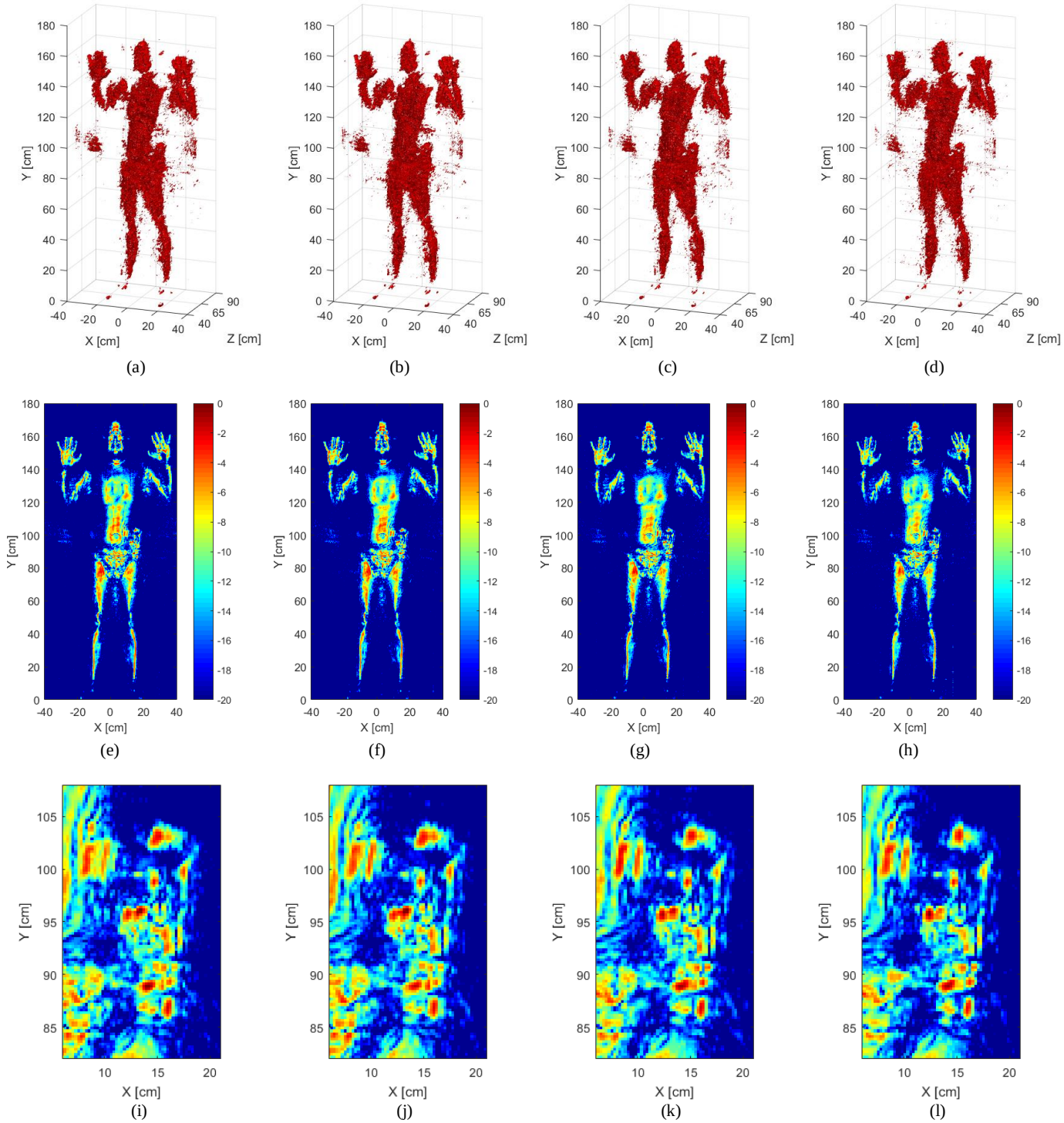

Fig. 12. Holographic reconstructions for the man shown in Fig. 10. (a) 3-D image by MIMO-FSA. (b) 3-D image by RMA. (c) 3-D image by SAR-FFT. (d) 3-D image by MIMO-EA. (e) Front view of (a). (f) Front view of (b). (g) Front view of (c). (h) Front view of (d). (i) Zoomed-in view of handgun in (e). (j) Zoomed-in view of handgun in (f). (k) Zoomed-in view of handgun in (g). (l) Zoomed-in view of handgun in (h). All results are displayed under the same dynamic level of -20 dB. Front views are obtained by maximum projection of 3-D image onto X-Y plane.

APPENDIX A
ACQUIREMENT OF THE WAVENUMBER DOMAIN SPECTRUM IN (3) WITH PSP

For the frequency domain wave sS in (1), a 2-D FT is first conducted over the x_T and x_R dimensions. Use PSP to solve the Fourier integral and yield

$$\begin{aligned}
&S_x s_y S\left(k_{xT}, k_{xR}; y_L; k\right) \\
&= \iint sS\left(x_T, x_R; y_L; k\right) \exp\left[-j\left(k_{xT}x_T + k_{xR}x_R\right)\right] dx_T dx_R \\
&= \iiint_V dxdydz \frac{1}{2} \exp\left(j\frac{\pi}{2}\right) f\left(x, y, z\right) P\left(k\right) \\
&\quad \times \frac{w_T\left[\dfrac{k_{xT}R_Y}{\sqrt{\left(k_0+k\right)^2 - k_{xT}^2}}, y - y_L\right] w_R\left[\dfrac{k_{xR}R_Y}{\sqrt{\left(k_0+k\right)^2 - k_{xR}^2}}, y - y_L\right]}{R_Y\left\{\left[\left(k_0+k\right)^2 - k_{xT}^2\right]\left[\left(k_0+k\right)^2 - k_{xR}^2\right]\right\}^{1/4}} \\
&\quad \times \exp\left\{-j\left[\left(k_{xT}+k_{xR}\right)x + k_{yz}R_Y\right]\right\}
\end{aligned} \tag{27}$$

where

$$R_Y = \sqrt{\left(y - y_L\right)^2 + z^2} \tag{28}$$

and

$$k_{yz} = \sqrt{\left(k_0+k\right)^2 - k_{xT}^2} + \sqrt{\left(k_0+k\right)^2 - k_{xR}^2} \tag{29}$$

while the stationary points are

$$x_{T0} = x - \frac{k_{xT}R_Y}{\sqrt{\left(k_0+k\right)^2 - k_{xT}^2}} \quad x_{R0} = x - \frac{k_{xR}R_Y}{\sqrt{\left(k_0+k\right)^2 - k_{xR}^2}} \tag{30}$$

Then, conduct a FT to $S_x s_y S$ over the y_L dimension. Also use PSP to solve the Fourier integral and yield

$$\begin{aligned}
&SS\left(k_{xT}, k_{xR}; y_L; k\right) \\
&= \int S_x s_y S\left(k_{xT}, k_{xR}; y_L; k\right) \exp\left(-jk_y y_L\right) dy_L \\
&= \iiint_V dxdydz \frac{\sqrt{2\pi}}{2} \exp\left(j\frac{3\pi}{4}\right) f\left(x, y, z\right) P\left(k\right) \\
&\quad \times \frac{w_T\left[\dfrac{k_{xT}k_{yz}z}{\sqrt{\left(k_0+k\right)^2 - k_{xT}^2}\sqrt{k_{yz}^2 - k_y^2}}, \dfrac{k_y z}{\sqrt{k_{yz}^2 - k_y^2}}\right] w_R\left[\dfrac{k_{xR}k_{yz}z}{\sqrt{\left(k_0+k\right)^2 - k_{xR}^2}\sqrt{k_{yz}^2 - k_y^2}}, \dfrac{k_y z}{\sqrt{k_{yz}^2 - k_y^2}}\right]}{\sqrt{z}\left\{\left[\left(k_0+k\right)^2 - k_{xT}^2\right]\left[\left(k_0+k\right)^2 - k_{xR}^2\right]\left(k_{yz}^2 - k_y^2\right)\right\}^{1/4}} \\
&\quad \times \exp\left\{-j\left[\left(k_{xT}+k_{xR}\right)x + k_y y + \sqrt{k_{yz}^2 - k_y^2}\, z\right]\right\}
\end{aligned} \tag{31}$$

and the stationary point is given as

$$y_{L0} = y - \frac{k_y z}{\sqrt{k_{yz}^2 - k_y^2}} \tag{32}$$

APPENDIX B
EXPANSION OF THE COUPLING PHASE TERM IN (3)

The coupling phase in (3) has the form as

$$\begin{aligned}\sqrt{k_{yz}^2-k_y^2}\,z &= z\sqrt{\left[\sqrt{\left(k_0+k\right)^2-k_{xT}^2}+\sqrt{\left(k_0+k\right)^2-k_{xR}^2}\right]^2-k_y^2} \\ &= z\sqrt{\left[k_0D_{Tx}\sqrt{1+\left(\frac{2k}{k_0}+\frac{k^2}{k_0^2}\right)\Big/D_{Tx}^2}+k_0D_{Rx}\sqrt{1+\left(\frac{2k}{k_0}+\frac{k^2}{k_0^2}\right)\Big/D_{Rx}^2}\right]^2-k_y^2}\end{aligned} \tag{33}$$

where the R-D domain squint functions

$$D_{Tx}=\sqrt{1-k_{xT}^2/k_0^2}\quad D_{Rx}=\sqrt{1-k_{xR}^2/k_0^2} \tag{34}$$

Expanding the inner two square root terms of (33) in a power series of k, and keeping terms up to k, then the phase becomes

$$\begin{aligned}\sqrt{k_{yz}^2-k_y^2}\,z &\approx z\sqrt{\left[k_0\left(D_{Tx}+D_{Rx}\right)+\frac{D_{Tx}+D_{Rx}}{D_{Tx}D_{Rx}}k\right]^2-k_y^2} \\ &\approx zk_0\left(D_{Tx}+D_{Rx}\right)\sqrt{1+g_{1x}k-\frac{k_y^2}{k_0^2\left(D_{Tx}+D_{Rx}\right)^2}} \\ &= zk_0\left(D_{Tx}+D_{Rx}\right)D_Y\sqrt{1+\frac{g_{1x}k}{D_Y^2}}\end{aligned} \tag{35}$$

where the coefficient

$$g_{1x}=\frac{2}{k_0D_{Tx}D_{Rx}} \tag{36}$$

and the R-D domain squint function

$$D_Y=\sqrt{1-\frac{k_y^2}{k_0^2\left(D_{Tx}+D_{Rx}\right)^2}} \tag{37}$$

The higher order terms missing from (35) can be ignored when

$$D_{Tx}^2\gg\left|\frac{2k}{k_0}+\frac{k^2}{k_0^2}\right|\quad D_{Rx}^2\gg\left|\frac{2k}{k_0}+\frac{k^2}{k_0^2}\right| \tag{38}$$

In the similar way, when

$$D_Y^2\gg\left|g_{1x}k\right| \tag{39}$$

the square root term of (35) can also be expanded in a power series of k, then retain terms up to k, thus we have

$$\sqrt{k_{yz}^2-k_y^2}\,z\approx\left(g_0+g_1k\right)z \tag{40}$$

where the R-D domain coefficients are

$$g_0=k_0D_Y\left(D_{Tx}+D_{Rx}\right)\quad g_1=\frac{D_{Tx}+D_{Rx}}{D_{Tx}D_{Rx}D_Y} \tag{41}$$

Note that, such an expansion retains all the terms no higher than the linear order of k from the original phase of (33).

APPENDIX C
DEMONSTRATION FOR (15)

The demonstration for (15) is as follows

$$\begin{aligned}
&SS_3\left(k_{xT},k_{xR},k_y;k\right)\\
&=\iiint_V dxdydz\times f\left(x,y,z\right)\exp\left\{-j\left[\left(k_{xT}+k_{xR}\right)x+k_y y\right]\right\}\\
&\quad\times\exp\left[-j\left(g_0+g_1 k\right)\left(z-z_0\right)\right]\otimes\exp\left(-j\frac{c^2k^2}{4K}\right)\exp\left[j\frac{c^2k^2}{4K}\left(1-\xi\right)\right]\\
&=\iiint_V dxdydz\times f\left(x,y,z\right)\exp\left\{-j\left[\left(k_{xT}+k_{xR}\right)x+k_y y\right]\right\}\exp\left[-jg_0\left(z-z_0\right)\right]\\
&\quad\times\int d\kappa\exp\left[-jg_1\kappa\left(z-z_0\right)\right]\exp\left[-j\frac{c^2\left(k-\kappa\right)^2}{4K}\right]\exp\left[j\frac{c^2k^2}{4K}\left(1-\xi\right)\right]\\
&=\iiint_V dxdydz\times f\left(x,y,z\right)\exp\left\{-j\left[\left(k_{xT}+k_{xR}\right)x+k_y y\right]\right\}\exp\left[-jg_0\left(z-z_0\right)\right]\\
&\quad\times\int d\kappa\exp\left[-jg_1\kappa\left(z-z_0\right)\right]\exp\left[j\frac{c^2\kappa^2}{4K}\left(\frac{1}{\xi}-1\right)\right]\exp\left[-j\frac{c^2}{4K}\left(\xi k^2-2k\kappa+\frac{1}{\xi}\kappa^2\right)\right]
\end{aligned}\tag{42}$$

Let $\kappa=\xi\kappa'$, then the function of (42) can be updated to

$$\begin{aligned}
&SS_3\left(k_{xT},k_{xR},k_y;k\right)\\
&=\iiint_V dxdydz\times f\left(x,y,z\right)\exp\left\{-j\left[\left(k_{xT}+k_{xR}\right)x+k_y y\right]\right\}\exp\left[-jg_0\left(z-z_0\right)\right]\\
&\quad\times\int d\xi\kappa'\exp\left[-jg_1\xi\kappa'\left(z-z_0\right)\right]\exp\left[j\frac{c^2\xi\kappa'^2}{4K}\left(1-\xi\right)\right]\exp\left[-j\frac{c^2\xi}{4K}\left(k-\kappa'\right)^2\right]
\end{aligned}\tag{43}$$

As ξ is independent of the range variable k, there is $d\xi\kappa'=\xi d\kappa'$, and thus we have

$$\begin{aligned}
&SS_3\left(k_{xT},k_{xR},k_y;k\right)\\
&=\iiint_V dxdydz\times\xi f\left(x,y,z\right)\exp\left\{-j\left[\left(k_{xT}+k_{xR}\right)x+k_y y\right]\right\}\exp\left[-jg_0\left(z-z_0\right)\right]\\
&\quad\times\int d\kappa'\exp\left[-jg_1\xi\kappa'\left(z-z_0\right)\right]\exp\left[j\frac{c^2\xi\kappa'^2}{4K}\left(1-\xi\right)\right]\exp\left[-j\frac{c^2\xi}{4K}\left(k-\kappa'\right)^2\right]\\
&=\iiint_V dxdydz\times\xi f\left(x,y,z\right)\exp\left\{-j\left[\left(k_{xT}+k_{xR}\right)x+k_y y\right]\right\}\exp\left[-jg_0\left(z-z_0\right)\right]\\
&\quad\times\exp\left[-jg_1\xi k\left(z-z_0\right)\right]\exp\left[j\frac{c^2\xi k^2}{4K}\left(1-\xi\right)\right]\otimes\exp\left(-j\frac{c^2\xi k^2}{4K}\right)
\end{aligned}\tag{44}$$

When ξ is equal to $\frac{2D_{Tx}D_{Rx}D_Y}{D_{Tx}+D_{Rx}}$, obviously (44) can be updated to

$$\begin{aligned}
&SS_3\left(k_{xT},k_{xR};k_y;k\right)\\
&=\iiint_V dxdydz\times\xi f\left(x,y,z\right)\exp\left\{-j\left[\left(k_{xT}+k_{xR}\right)x+k_y y+2k\left(z-z_0\right)\right]\right\}\\
&\quad\times\exp\left[-jg_0\left(z-z_0\right)\right]\exp\left[j\frac{c^2\xi k^2}{4K}\left(1-\xi\right)\right]\otimes\exp\left(-j\frac{c^2\xi k^2}{4K}\right)
\end{aligned}\tag{45}$$

This is exactly the same as the expression in (15).

Q.E.D.

ACKNOWLEDGEMENT

First of all, the authors would like to thank the anonymous reviewers very warmly for their detailed comments and suggestions. Then, K. Tan would like to thank Ms. Q. Wang of the Institute of Electronics, Chinese Academy of Sciences, and Ph.D. candidate Y. Zhou of the Department of Electrical and Computer Engineering, National University of Singapore, for their great help of this work.

REFERENCES

[1] H. D. Collins, D. L. McMakin, T. E. Hall, and R. P. Gribble, "Real-time holographic surveillance system," U.S. Patent 5 455 590, Oct. 3, 1995.

[2] R. Appleby and R. N. Anderton, "Millimeter-Wave and Submillimeter-Wave Imaging for Security and Surveillance," *Proc. IEEE*, vol. 95, no. 8, pp. 1683-1690, Aug. 2007.

[3] J. H. Wehling, "Multifunction millimeter-wave systems for armored vehicle application," *IEEE Trans. Microw. Theory Techn.*, vol. 53, no. 3, pp. 1021-1025, Mar. 2005.

[4] J. Gonzalez-Partida, P. Almorox-Gonzalez, M. Burgos-Garcia, B. Dorta-Naranjo and J. I. Alonso, "Through-the-Wall Surveillance With Millimeter-Wave LFMCW Radars," *IEEE Trans. Geosci. Remote Sens.*, vol. 47, no. 6, pp. 1796-1805, Jun. 2009.

[5] U. Alkus, A. B. Sahin and H. Altan, "Stand-Off Through-the-Wall W-Band Millimeter-Wave Imaging Using Compressive Sensing," *IEEE Geosci. Remote Sens. Lett.*, vol. 15, no. 7, pp. 1025-1029, Jul. 2018.

[6] N. H. Farhat and W. R. Guard, "Millimeter wave holographic imaging of concealed weapons," *Proc. IEEE*, vol. 59, pp. 1383–1384, Sept. 1971.

[7] D. M. Sheen, D. L. McMakin, and T. E. Hall, "Three-dimensional millimeter-wave imaging for concealed weapon detection," *IEEE Trans. Microw. Theory Techn.*, vol. 49, no. 9, pp. 1581–1592, Sep. 2001.

[8] X. Zhuge and A. G. Yarovoy, "A sparse aperture MIMO-SAR-based UWB imaging system for concealed weapon detection," *IEEE Trans. Geosci. Remote Sens.*, vol. 49, no. 1, pp. 509–518, Jan. 2011.

[9] J. Grajal, *et al*., "3-D High-Resolution Imaging Radar at 300 GHz With Enhanced FoV," *IEEE Trans. Microw. Theory Techn.*, vol. 63, no. 3, pp. 1097-1107, Mar. 2015.

[10] N. Hoshi, Y. Nikawa, K. Kawai and S. Ebisu, "Application of microwaves and millimeter waves for the characterization of teeth for dental diagnosis and treatment," *IEEE Trans. Microw. Theory Techn.*, vol. 46, no. 6, pp. 834-838, June 1998.

[11] A. Mirbeik-Sabzevari, E. Oppelaar, R. Ashinoff and N. Tavassolian, "High-Contrast, Low-Cost, 3-D Visualization of Skin Cancer Using Ultra-High-Resolution Millimeter-Wave Imaging," *IEEE Trans. Med. Imag.*, vol. 38, no. 9, pp. 2188-2197, Sept. 2019.

[12] A. Bellossi, G. Dubost, J. P. Moulinoux, M. Himdi, M. Ruelloux and C. Rocher, "Biological effects of millimeter wave irradiation on mice-preliminary results," *IEEE Trans. Microw. Theory Techn.*, vol. 48, no. 11, pp. 2104-2110, Nov. 2000.

[13] M. Zhadobov, R. Sauleau, V. Vie, M. Himdi, L. Le Coq and D. Thouroude, "Interactions between 60-GHz millimeter waves and artificial biological membranes: dependence on radiation parameters," *IEEE Trans. Microw. Theory Techn.*, vol. 54, no. 6, pp. 2534-2542, Jun. 2006.

[14] F. Gumbmann and L. Schmidt, "Millimeter-Wave Imaging With Optimized Sparse Periodic Array for Short-Range Applications," *IEEE Trans. Geosci. Remote Sens.*, vol. 49, no. 10, pp. 3629-3638, Oct. 2011.

[15] S. S. Ahmed, A. Schiessl, and L.-P. Schmidt, "A novel fully electronic active real-time imager based on a planar multistatic sparse array," *IEEE Trans. Microw. Theory Techn.*, vol. 59, no. 12, pp. 3567–3576, Dec. 2011.

[16] H. Zamani and M. Fakharzadeh, "1.5-D Sparse Array for Millimeter-Wave Imaging Based on Compressive Sensing Techniques," *IEEE Trans. Antennas Propag.*, vol. 66, no. 4, pp. 2008-2015, Apr. 2018.

[17] B. Cheng, *et al*., "340-GHz 3-D Imaging Radar With 4Tx-16Rx MIMO Array," *IEEE Trans. Terahertz Science and Technology*, vol. 8, no. 5, pp. 509-519, Sept. 2018.

[18] J. Gao, B. Deng, Y. Qin, H. Wang and X. Li, "An Efficient Algorithm for MIMO Cylindrical Millimeter-Wave Holographic 3-D Imaging," *IEEE Trans. Microw. Theory Techn.*, vol. 66, no. 11, pp. 5065-5074, Nov. 2018.

[19] Z. Wang, Q. Guo, X. Tian, T. Chang and H. Cui, "Near-Field 3-D Millimeter-Wave Imaging Using MIMO RMA With Range Compensation," *IEEE Trans. Microw. Theory Techn.*, vol. 67, no. 3, pp. 1157-1166, Mar. 2019.

[20] X. Chen, *Computational Methods for Electromagnetic Inverse Scattering*. Wiley-IEEE, 2018.

[21] X. Zhuge, A. G. Yarovoy, T. G. Savelyev and L. P. Ligthart, "Modified Kirchhoff Migration for UWB MIMO Array-Based Radar Imaging," *IEEE Trans. Geosci. Remote Sens.*, vol. 48, no. 6, pp. 2692-2703, Jun. 2010.

[22] X. Zhuge and A. G. Yarovoy, "Three-Dimensional Near-Field MIMO Array Imaging Using Range Migration Techniques," *IEEE Trans. Image Process.*, vol. 21, no. 6, pp. 3026-3033, June 2012.

[23] K. Tan, S. Wu, X. Liu and G. Fang, "A Modified Omega-K Algorithm for Near-Field MIMO Array-Based 3-D Reconstruction," *IEEE Geosci. Remote Sens. Lett.*, vol. 15, no. 10, pp. 1555-1559, Oct. 2018.

[24] K. Tan, S. Wu, X. Liu and G. Fang, "Omega-K Algorithm for Near-Field 3-D Image Reconstruction Based on Planar SIMO/MIMO Array," *IEEE Trans. Geosci. Remote Sens.*, vol. 57, no. 4, pp. 2381-2394, Apr. 2019.

[25] J. Zhou, R. Zhu, G. Jiang, L. Zhao and B. Cheng, "A Precise Wavenumber Domain Algorithm for Near Range Microwave Imaging by Cross MIMO Array," *IEEE Trans. Microw. Theory Techn.*, vol. 67, no. 4, pp. 1316-1326, Apr. 2019.

[26] Q. Guo, J. Liang, T. Chang and H. Cui, "Millimeter-Wave Imaging With Accelerated Super-Resolution Range Migration Algorithm," *IEEE Trans. Microw. Theory Techn.*, vol. 67, no. 11, pp. 4610-4621, Nov. 2019.

[27] T. Fromenteze, O. Yurduseven, F. Berland, C. Decroze, D. R. Smith and A. G. Yarovoy, "A Transverse Spectrum Deconvolution Technique for MIMO Short-Range Fourier Imaging," *IEEE Trans. Geosci. Remote Sens.*, vol. 57, no. 9, pp. 6311-6324, Sept. 2019.

[28] R. Zhu, J. Zhou, G. Jiang and Q. Fu, "Range Migration Algorithm for Near-Field MIMO-SAR Imaging," *IEEE Geosci. Remote Sens. Lett.*, vol. 14, no. 12, pp. 2280-2284, Dec. 2017.

[29] J. Gao, Y. Qin, B. Deng, H. Wang and X. Li, "Novel Efficient 3D Short-Range Imaging Algorithms for a Scanning 1D-MIMO Array," *IEEE Trans. Image Process.*, vol. 27, no. 7, pp. 3631-3643, July 2018.

[30] M. Abbasi, A. Shayei, M. Shabany and Z. Kavehvash, "Fast Fourier-Based Implementation of Synthetic Aperture Radar Algorithm for Multistatic Imaging System," *IEEE Trans. Instrum. Meas.*, vol. 68, no. 9, pp. 3339-3349, Sept. 2019.

[31] I. G. Cumming and F. H. Wong, *Digital processing of Synthetic Aperture Radar Data Algorithms and Implementation*. Norwood, MA: Artech House, 2005.